Accelerating ion diffusion with unique three-dimensionally interconnected nanopores for self-membrane high-performance pseudocapacitors†

Yuan Gao, [ID] [a] Yuanjing Lin, [ID] [a] Zehua Peng, [b] Qingfeng Zhou [c] and Zhiyong Fan [ID] *[a]

Herein, a unique three-dimensionally interconnected nanoporous structure (3-D INPOS) pseudocapacitor electrode, which possesses a large surface area, an efficient electron and ion transport, together with a remarkable structural stability, has been constructed *via* soft anodization of an aluminum alloy, cost-effective ultrasonic spray pyrolysis (USP)-assisted deposition of fluorine-doped tin oxide (FTO), and controllable electrochemical deposition of nanostructured manganese dioxide (MnO_2). Taking the advantage of large surface area, the as-built 3-D INPOS pseudocapacitor electrode exhibits the highest areal capacitance of 540 mF cm^{-2} and a volumetric capacitance of 135 F cm^{-3}, which is 53% higher than that achieved from the conventional 3-D nanopore pseudocapacitor electrode and 17.6 times higher than that of the planar electrode. More interestingly, the unique 3-D interconnected structure offers an unrestricted space for the diffusion of electrolyte ions. Thus, the 3-D INPOS electrode achieves a higher rate capability than the 3-D nanopore electrode. As a proof of concept, a symmetric self-membrane pseudocapacitor device was constructed by simply stacking two pieces of the 3-D INPOS electrodes. Without an added separator, the device possesses a largely reduced dead volume and achieves the highest volumetric capacitance of 28.9 F cm^{-3} and a specific energy of 2.36 mW h cm^{-3}. The largely enhanced capacitance, rate capability, and specific energy certainly make the 3-D INPOS an ideal architecture for the fabrication of high-performance pseudocapacitors.

Introduction

The energy and environmental crisis arising from burning fossil fuels have made the utilization of renewable energy significantly important.[1-3] Electrochemical energy storage devices, such as batteries and supercapacitors, are capable of converting the electricity produced by solar radiation, waves, and wind into electrochemical energy and releasing this energy elsewhere. Moreover, these electrochemical energy storage devices can compensate the intermittency of renewable energy sources.[4] Especially, supercapacitors possess appealing features such as higher specific power, faster charging–discharging rate, and much longer cyclic lifetime than rechargeable batteries, thus offering possibilities in a broad range of energy-related applications such as regenerative breaks in electric vehicles, memory backup systems, and pacemakers in medical

[a]*Department of Electronic and Computer Engineering, The Hong Kong University of Science and Technology, Clear Water Bay, Kowloon, Hong Kong, China SAR.*
E-mail: eezfan@ust.hk
[b]*Institute of Textiles and Clothing, The Hong Kong Polytechnic University, Hung Hom, Hong Kong SAR, China*
[c]*School of Computer and Information, Hefei University of Technology, Hefei, China*
†Electronic supplementary information (ESI) available. See DOI: 10.1039/c7nr06234f

treatment.[5,6] To date, it is widely accepted that supercapacitors store energy *via* surface electrochemical activities including either physical ion adsorption or chemical redox reaction; thus, the electrochemical performance largely depends on the surface area of the supercapacitor electrode.[5] Particularly, for pseudocapacitors, current collectors with a large surface area are highly preferred for loading a large amount of active materials and to promote more surface redox reaction.[7] Extensive research has shown that the nanostructured architectures have a large surface-to-volume ratio. Therefore, fabrication of pseudocapacitor electrodes with nanostructures is certainly one of the most effective approaches to achieve high capacitance energy storage devices.[8-13] In particular, three-dimensional (3-D) nanostructured pseudocapacitors have been targeted as promising energy storage devices due to their large surface/interface area, allowing the deployment of pseudo-capacitive materials with nano/micro feature sizes.[14] As a result, pseudocapacitor electrodes fabricated based on 3-D nanowires (NWs), nanotubes (NTs), nanospikes (NSPs), and nanopillars (NPLs)[7,15-22] have been broadly explored. These structures have already demonstrated a decent capacitance and an efficient electron transport. However, due to lack of support from the neighboring structures, these 3-D arrays suffer from structural instability, especially those with a high aspect ratio (AR). Agglomeration of 3-D arrays results in a

largely reduced surface area and capacitance loss. In this regard, recent reports have demonstrated that 3-D nickel (Ni) nanopores can achieve AR higher than 24 with a remarkable mechanical strength, which addresses the collapse issue.[23,24] However, Ni nanopores require thick side walls to maintain their freestanding architecture and thus lead to a reduced available surface area. Moreover, this long-range nanoconfined architecture impedes the transport of the electrolyte ions. Both of these impose adverse effects on the pseudocapacitor performance; and this makes the 3-D nanopores still far from the ideal structure. Thus, the ideally 3-D nanostructure should possess the virtues of a large surface area, an excellent structural stability, and an unrestricted space for the transport of electrolyte ions.

To achieve this architecture, we have successfully engineered a 3-D interconnected nanoporous structure (INPOS) via unconventional anodization of aluminum (Al) alloy. In this architecture, straight anodic aluminum oxide (AAO) channels are formed via self-organizing mechanism,[25] and the nanovoids are distributed uniformly on the side wall of all nanochannels. Moreover, these nanovoids can be further developed into lateral branch-like voids, which penetrate through the AAO side walls by chemical etching, hence forming the highly porous and mechanically stable 3-D INPOS. With the cost-effective ultrasonic spray pyrolysis (USP) method, fluorine-doped tin oxide (FTO) was successfully deposited onto the 3-D INPOS with a length of 40 μm (AR of 80) to complete the fabrication of the 3-D INPOS current collector. After the controllable deposition of manganese dioxide (MnO_2) via the electrochemical deposition (ED), the as-built 3-D INPOS pseudocapacitor electrodes achieved the highest areal capacitance of 540 mF cm^{-2} and the volumetric capacitance of 135 F cm^{-3} at the discharging current density of 0.1 mA cm^{-2} and still maintained the values of 367.8 mF cm^{-2} and 92 F cm^{-3}, respectively, at the discharging current density of 1.5 mA cm^{-2}. In contrast, the values obtained from the conventional 3-D nanopore electrodes are only 353 mF cm^{-2} and 88.3 F cm^{-3}, and these performances drastically degrade to 52.2 mF cm^{-2} and 13.1 F cm^{-3}, respectively, with the increasing discharging current density. The performance improvement is even larger as compared to that of the planar pseudocapacitor electrode. In addition, a self-membrane pseudocapacitor device was constructed by assembling two pieces of the 3-D INPOS electrodes without further addition of a separator, and a largely enhanced device volumetric capacitance of 28.9 F cm^{-3} and the specific energy of 2.36 mW h cm^{-3} at the discharging current density of 0.1 mA cm^{-2} were obtained.

Results and discussion

The schematics of the as-built 3-D INPOS pseudocapacitor electrodes are shown in Fig. 1. The fabrication mainly consists of three steps: (a) soft anodization of the Al alloy and chemically wet etching to achieve the through-hole 3-D INPOS with a pitch of 500 nm, (b) the USP-assisted conformal and uniform
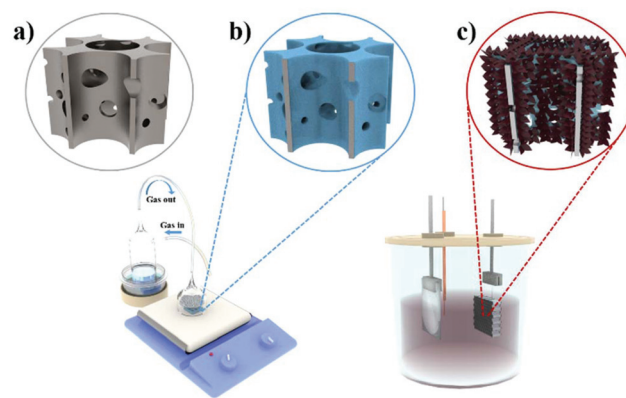

Fig. 1 Schematic of the fabrication process of the 3-D INPOS pseudocapacitor electrodes: (a) the 3-D INPOS architecture achieved after anodization of the Al alloy and chemically pore widening, (b) the USP of FTO to achieve the 3-D INPOS current collectors, and (c) the ED of MnO_2 to achieve the 3-D INPOS pseudocapacitor electrodes.

deposition of FTO inside the INPOS to obtain the conductive 3-D INPOS current collectors, and this method has been systematically studied in our previous report,[7] and (c) the homogeneous ED of MnO_2 nanowires into the 3-D INPOS current collectors to complete the fabrication of the pseudocapacitor electrodes. It is worth mentioning that to obtain 3-D INPOS current collectors, the USP method has been adopted to deposit FTO onto the 3-D INPOS scaffold with a certain uniformity, and this method is superior to atomic layer deposition (ALD) and physical vapor deposition (sputter and evaporator) in longer nanochannels deposition with an excellent cost-effectiveness.[7,17,24,26] As an evidence, a 3-D INPOS current collector with a thickness of 40 μm (nanochannels with AR of 80) was successfully constructed, as shown in Fig. S1.†

Fig. 2a and b show the scanning electron microscopy (SEM) images of the structural difference between the 3-D nanopores and the 3-D INPOS. Particularly, for the 3-D nanopores, as shown in Fig. 2a, the highly packed AAO structures are formed by self-assembly mechanism, and their corresponding morphological parameters, namely length, diameter, and pitch, can be facilely tuned by anodization duration, applied voltage, as well as etching time.[27] In contrast, the unique 3-D INPOS architectures are obtained by the formation of nanovoids on the side wall of nanochannels, and these nanovoids distribute uniformly in all AAO channels during the anodization of the Al alloy, as shown in Fig. 2b and Fig. S2.† These nanovoids are formed during anodization due to the copper (Cu) impurity in the Al alloy. The formation mechanism for this impurity-driven nanovoid has been unveiled in another report.[28] Moreover, these nanovoids can be further turned into the branch-like voids that connect the neighboring AAO nanochannels laterally after chemically pore widening, thus leading to the formation of a unique 3-D INPOS architecture. Noteworthily, the 3-D INPOS not only maintains the excellent mechanical stability of the 3-D nanopores but is also superior to the 3-D nanopores in terms of the larger surface area due to
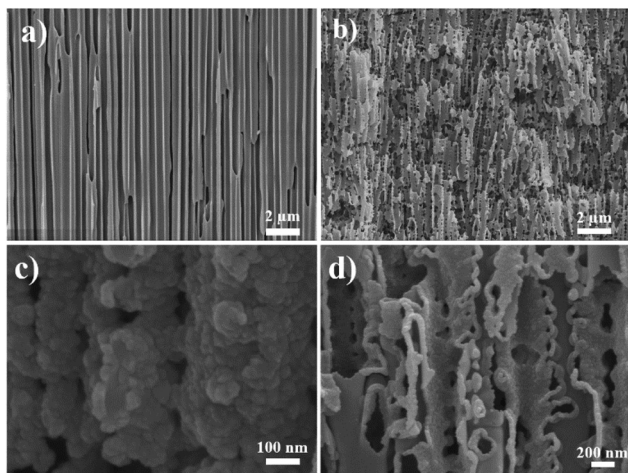
Fig. 2 SEM images of the structural morphologies for the 3-D nano-pores and the 3-D INPOS architectures. (a–b) Low-resolution SEM images of the 3-D nanopores and the 3-D INPOS. (c) High resolution SEM images of the 3-D INPOS after FTO deposition. (d) The 3-D INPOS after the removal of the AAO scaffold.

its highly porous structure. To fabricate the 3-D INPOS current collectors, FTO was deposited onto the 3-D INPOS scaffold *via* the cost-effective USP method, as shown in Fig. 2c and Fig. S1.† Although covered with a layer of FTO, as shown in Fig. 2c, this structure still maintains the interconnected nanopores. Moreover, FTO with the same thickness was deposited onto the 3-D nanopores with the same length of channel for the structural comparison, as shown in the SEM images in Fig. S2.† Interestingly, the 3-D nanopores render a sheet resistance of 161 Ω sq^{-1}, whereas the value for the 3-D INPOS is only 25 Ω sq^{-1}. To investigate the reason for the largely reduced resistance, the as-built 3-D INPOS was immersed in 1 M sodium hydroxide (NaOH) to remove the AAO backbone. Apparently, a highly porous and three-dimensionally inter-connected FTO structure was exposed after the AAO backbone was removed, and this 3-D architecture was both mechanically and electrically connected, as shown in Fig. 2d. In comparison, without the formation of the three-dimensionally inter-connected FTO inside the channels, the 3-D nanopores possess much less electrically conductive pathway, which leads to a higher sheet resistance.

To explore the feasibility of utilization of this architecture as a pseudocapacitor electrode, the 3-D INPOS current collectors with the average length, diameter, and pitch of 40 μm, 260 nm, and 400 nm, respectively, (as shown in Fig. S1†) were adopted to load different amounts of MnO$_2$. A time controllable galvanostatic ED was applied to homogenously deposit MnO$_2$ onto the 3-D INPOS current collectors with the loading amount of 0.697 mg cm^{-2}, 1.046 mg cm^{-2}, 1.744 mg cm^{-2}, and 2.441 mg cm^{-2}. The chemical components of the 3-D INPOS pseudocapacitor electrode were characterized by energy dispersive spectrometer (EDS), as shown in Fig. S4.† It is clearly indicated that with the increasing deposition time, the 3-D INPOS current collectors are gradually filled with the nano-

wire-like active material, however, the highly porous structure is still maintained even with a large mass loading of 2.441 mg cm^{-2}, as shown in Fig. 3a and b and Fig. S5.† In contrast, the 3-D nanopore pseudocapacitor electrode achieves the more compact MnO$_2$ nanowires inside the channels and this results in a tiny open pore size, as shown in Fig. 3c and d. To make a further comparison, the commercialized FTO glass was adopted to serve as the planar current collector for the depo-sition of 2.441 mg cm^{-2} MnO$_2$, and the result clearly showed that a dense MnO$_2$ film with the thickness of 12 μm was deposited onto the planar current collector, and the nano-structured MnO$_2$ could only be seen from the top layer, as shown in Fig. 3e and f. The reason for this intriguing phenom-enon is that the 3-D INPOS has a larger surface area than 3-D nanopores and the planar current collectors, which enables loading less compact nanostructured active materials.

To assess the electrochemical performance of the 3-D INPOS pseudocapacitor electrode, cyclic voltammetry (CV) and galvanostatic charging–discharging (GCD) measurements were conducted based on a three-electrode configuration. Fig. 4a shows the CV curves of the 3-D INPOS electrodes with different amounts of MnO$_2$ deposition at a scan rate of 50 mV s^{-1}. Apparently, the area enclosed by the CV curves enlarges with the increasing deposition time and reaches the peak value at the deposition amount of 2.441 mg cm^{-2}. The largest CV area
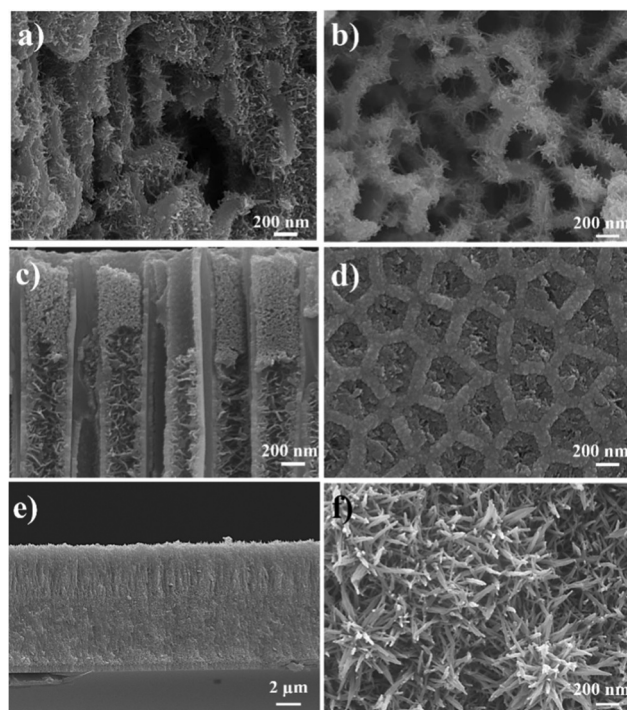

Fig. 3 (a–b) Side view and top view SEM images of the 3-D INPOS pseudocapacitor electrodes with the deposition amount of 2.441 mg cm^{-2}. (c–d) Side view and top view SEM images of the 3-D nanopore pseudocapacitor electrodes with the deposition amount of 2.441 mg cm^{-2}. (e–f) Side view and top view SEM images of the planar pseudo-capacitor electrodes with the deposition amount of 2.441 mg cm^{-2}. All the deposition amount densities are normalized to the footprint area.
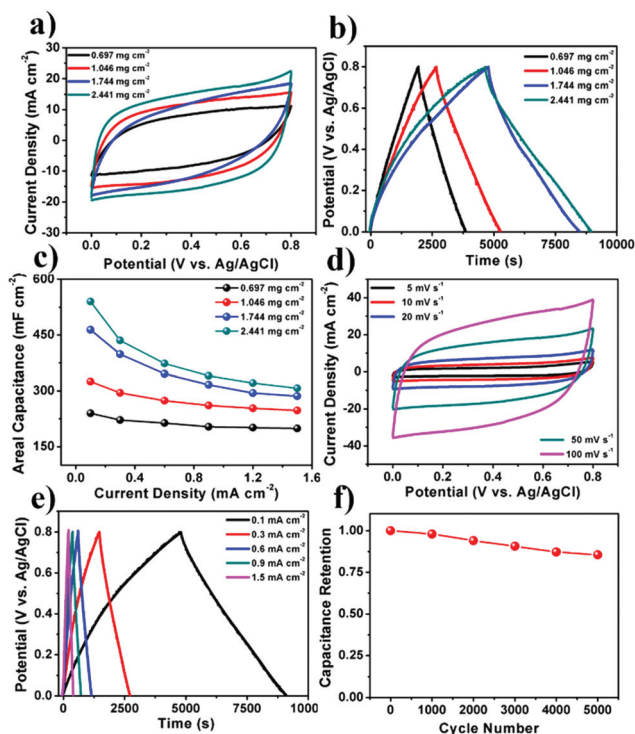
Fig. 4 (a) The CV curves of the 3-D INPOS electrodes with different mass loadings at the scan rate of 50 mV s⁻¹. (b) The GCD curves of the 3-D INPOS electrodes with different mass loadings at the discharging current density of 0.1 mA cm⁻². (c) Areal capacitance as a function of current densities. (d−e) The CV and GCD curves of the 3-D INPOS electrode with 2.441 mg cm⁻² mass loading. (f) The cyclic lifetime test for the 3-D INPOS electrode at the scan rate of 100 mV s⁻¹.

together with the longest discharging time, as shown in Fig. 4b, confirms that the 3-D INPOS pseudocapacitor electrode with the deposition amount of 2.441 mg cm⁻² has the highest capacitance. To conduct a systematic study, the CV curves of different amounts of MnO_2 deposition at different scan rates and the GCD curves with different discharging current densities are also plotted in Fig. S6–8.† Fig. 4c shows the relationship between areal capacitance and discharging current densities. The 3-D INPOS pseudocapacitor electrode with the deposition amount of 2.441 mg cm⁻² achieves the highest areal capacitance of 540 mF cm⁻² at the discharging current density of 0.1 mA cm⁻² and still maintains the value of 367.8 mF cm⁻² at the discharging current density of 1.5 mA cm⁻², which exhibits excellent rate capability. Therefore, this electrode was regarded as the optimized pseudo-capacitor electrode. Fig. 4d and e show the detailed CV and GCD curves of the optimized 3-D INPOS electrode. The mirror-like rectangular shape and linear voltage-time profile demonstrate its excellent pseudocapacitive behavior. To confirm that the capacitance mainly originates from the redox reaction, the CV comparison between the bare 3-D INPOS current collector and the 3-D INPOS pseudocapacitor electrode has also been carried out, as plotted in Fig. S9.† In addition, the gravimetric capacitance of the pseudocapacitor electrodes with different

mass loadings is also plotted, as shown in Fig. S6–9,† and the detailed capacitance calculation method is shown in eqn (S1)–(S4).† Noteworthily, the cyclic lifetime largely determines the reliability and practicality of pseudocapacitor electrodes, and this property is plotted in Fig. 4f. The result shows that the capacitance remains 98% of its initial value after 1000 cycles test and still maintains 85.5% of its initial value after 5000 cycles test. This high capacitance retention further proves the remarkable electrochemical performance of the 3-D INPOS pseudocapacitor electrode.

To further evaluate the merits of the 3-D INPOS electrode, the electrochemical performance of the 3-D nanopore electrode and the planar electrode was also studied. For the sake of a fair comparison, all the electrodes have the same geometry area and the same amount of MnO_2 loading (2.441 mg cm⁻²). Fig. 5a presents the comparison among the CV curves at the scan rate of 50 mV s⁻¹. The more symmetrical rectangular shape and larger area compassed by the CV curves prove the best electrochemical performance of the 3-D INPOS electrode. In addition, the GCD profile shows that during the discharging process, the 3-D INPOS electrode achieves the lowest voltage
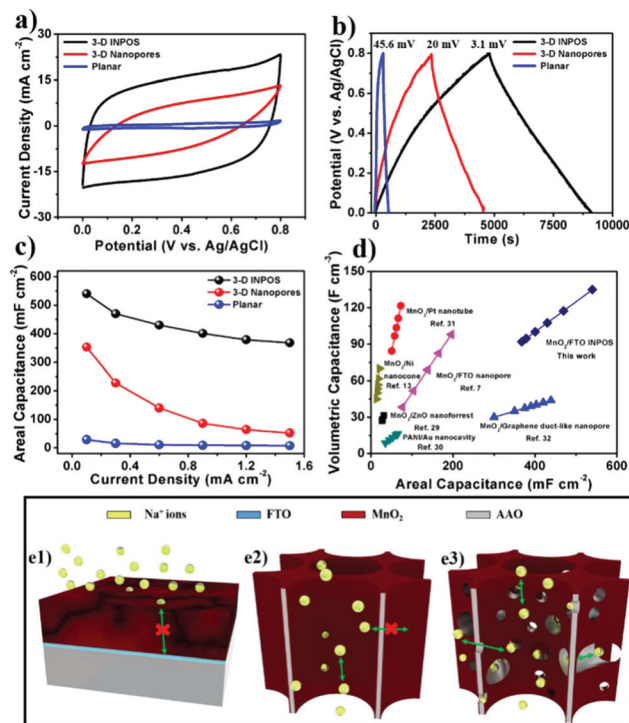

Fig. 5 (a) CV curves comparison among the 3-D INPOS electrode, the nanopore electrode, and the planar electrode at the scan rate of 50 mV s⁻¹. (b) The GCD curves comparison among the 3-D INPOS electrode, the nanopore electrode, and the planar electrode at the discharging current density of 0.1 mA cm⁻². (c) Areal capacitance of different electrodes as a function of discharging current densities. (d) Volumetric capacitance *versus* areal capacitance of the 3-D INPOS electrode in comparison with other values reported in the literature. (e) Schematic for the diffusion mechanisms of the electrolyte ions in different electrodes, including (e1) the planar electrode, (e2) the 3-D nanopore electrode, and (e3) the 3-D INPOS electrode.

drop of 3.1 mV in comparison with the 3-D nanopore electrode (20 mV) and the planar electrode (45.6 mV). This result suggests that the 3-D INPOS electrode obtains the lowest internal resistance and highest Coulombic efficiency. The areal capacitance as a function of discharging current densities is plotted in Fig. 5c. It is worth mentioning that the 3-D INPOS electrode achieves the highest areal capacitance of 540 mF cm^{-2} at the discharging current density of 0.1 mA cm^{-2} and still maintains the value of 367.8 mF cm^{-2} at the discharging current density of 1.5 mA cm^{-2}. In contrast, the areal capacitance obtained from the 3-D nanopore electrode is only 353 mF cm^{-2}, and this value sharply decreases to 52.2 mF cm^{-2} at the current density of 1.5 mA cm^{-2}. The detailed electrochemical performance of the 3-D nanopore electrode is shown in Fig. S10.† The areal capacitance achieved based on the planar electrode is even lower, which is 29 mF cm^{-2} and 8 mF cm^{-2}. The significant enhancement of the electrochemical performance of the 3-D INPOS electrode *versus* that of the 3-D nanopore electrode is further testified by the electrochemical impedance spectroscopy (EIS) measurements in the frequency range from 100 kHz to 0.01 Hz, as shown in Fig. S11.† The results show that the 3-D INPOS electrode presents the smallest radius of semicircle in the high-frequency region, demonstrating the lowest charge transfer impedance. Moreover, the smallest portion of Warburg impedance region at low frequency further proves that the 3-D INPOS electrode has the lowest diffusion impedance of the electrolyte ions. Notably, the promising 3-D nanostructured pseudocapacitor electrode should be able to achieve both high volumetric and areal capacitance, and this figure-of-merit is shown in Fig. 5d, benchmarking with the literature reported results for the same category of devices. It is apparent that our 3-D INPOS electrode with the highest areal capacitance of 540 mF cm^{-2} and the volumetric capacitance of 135 F cm^{-3} is superior to many other devices reported in the literature to a large extent.[13,29–32]

To shed light on the reason for the largely enhanced electrochemical performance, the proposed schematic of the diffusion mechanisms of the electrolyte ions for different electrodes is shown in Fig. 5e. Particularly, for the planar electrode, most of the ion diffusion is inhibited by the dense and thick active material, and the electrochemically active site is largely reduced, leading to low capacitance. In addition, the active materials loaded on the planar electrodes lack protection from the nanostructured backbone, and they cannot withstand volume expansion during the charging–discharging process, as shown in Fig. S12.† Thus, the pulverization of active materials results in the severe electrochemical performance degradation. As for the nanostructured electrode, the 3-D nanopore electrode offers a larger surface area for the deposition of active materials with nanoscale particle sizes. Thus, the electrolyte ions are accessible to the deeper structure *via* the interstice of the active materials, which is in favor of more charge storage. However, these ions are trapped in each nanopore, forming the one-dimensionally (1-D) vertical diffusion pathway and resulting in the sluggish ion diffusion and limited rate capability. In comparison, the 3-D INPOS electrode

renders a higher areal capacitance and a better rate capability, which can be ascribed to its unique structural properties: (i) the branch-like voids largely reduce the volume occupied by AAO and release more space for the deposition of the hierarchical active material, namely MnO$_2$ nanowires, thus increasing the electrolyte contact surface area and (ii) with the existence of the side pores, the electrolyte ions are capable to move freely into the neighboring channels and diffuse faster in the 3-D directions. It is worth emphasizing that due to these merits, the 3-D INPOS architecture is applicable to a broad range of classical pseudocapacitive materials such as polyaniline (PANI), polypyrrole (PPY), ruthenium dioxide (RuO$_2$), and any other types of pseudocapacitive materials as long as they can be deposited onto our 3-D architecture.

Typically, the volumetric capacitance and specific energy are determined by the pseudocapacitor device volume. In the conventional sandwich pseudocapacitor device, which consists of two electrodes and a separator, thinning or removal of separator is the most promising way to decrease the device dead volume without sacrificing the device capacitance. To exemplify this concept, a symmetric self-membrane pseudocapacitor device was constructed based on the 3-D INPOS electrodes. In this device configuration, two pieces of the 3-D INPOS electrodes with the thickness of 20 μm for each one were directly assembled without further addition of a separator, as shown in Fig. 6c. As is well-known, AAO has high porosity, large band gap, and excellent ionic conductivity, which is capable to serve as a separator in energy storage devices.[36] In the study presented herein, FTO and MnO$_2$ are deposited inside the 3-D INPOS, a kind of AAO, and the outer surface of the 3-D INPOS is left insulated for electrons but permeable for ions. In this scenario, the 3-D INPOS can work as both a
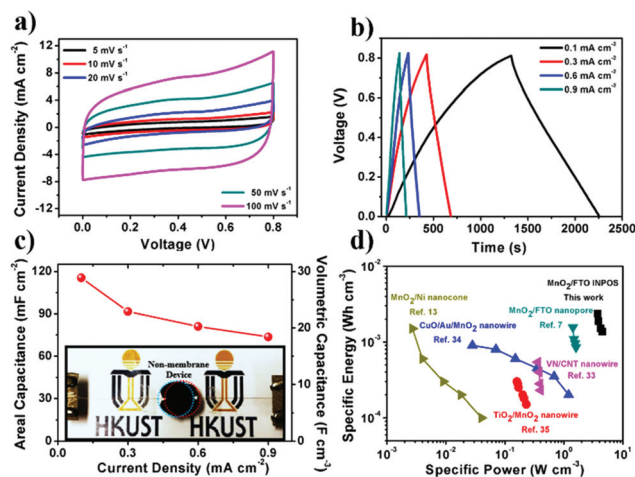

Fig. 6 (a–b) The CV and GCD curves of the self-membrane pseudocapacitor device. (c) Areal capacitance and volumetric capacitance as the functions of discharging current density. The inset image shows the symmetric self-membrane device. The blue and red dashed circles present two electrodes, and these electrodes are electrically connected to copper cables by a silver paste for electrochemistry measurements. (d) Ragone plot.

pseudocapacitor electrode and a separator, which results in the largely reduced device volume. As a result, the symmetric self-membrane pseudocapacitor achieves the highest volumetric capacitance of 28.9 F cm^{-3} at the discharging current density of 0.1 mA cm^{-2} and still maintains the value of 18.4 F cm^{-3} at the discharging current density of 1.5 mA cm^{-2}, as shown in Fig. 6c, and this value is among the highest values when compared with other results reported in the literatures, as shown in Fig. S13.† As seen in the Ragone plot shown in Fig. 6d, the self-membrane device achieves the highest specific energy and the specific power of 2.36 mW h cm^{-3} and 4.45 W h cm^{-3}, respectively, and these values outperform those of most of the symmetric pseudocapacitor devices and are even better than those of many asymmetric devices.[7,13,33–35]

Conclusions

In summary, we report a unique 3-D INPOS architecture constructed *via* anodization of an Al alloy. This structure inherits all the structural merits, including a large surface area, an efficient electron transport, as well as a good structural stability, of the 3-D nanopores, and is superior to the 3-D nanopores as it has a higher porosity and a better ion accessibility. The 3-D INPOS pseudocapacitor electrode built based on this architecture achieves the highest areal capacitance of 540 mF cm^{-2} together with the volumetric capacitance of 135 F cm^{-3} at the discharging current density of 0.1 mA cm^{-2} and still maintains the value of 367.8 mF cm^{-2} and 92 F cm^{-3} at the discharging current density of 1.5 mA cm^{-2}. In contrast, the values obtained from the 3-D nanopore electrode are only 353 mF cm^{-2} (88.3 F cm^{-3}) and 52.2 mF cm^{-2} (13.1 F cm^{-3}). The largely enhanced rate capability stems from the unrestricted ion diffusion pathway inside the 3-D INPOS electrode. Furthermore, a self-membrane pseudocapacitor device was constructed by simply stacking two pieces of the electrodes. Benefiting from the largely reduced dead volume, the device achieves the highest volumetric capacitance of 28.9 F cm^{-3} and the highest specific energy of 2.36 mW h cm^{-3}. With the merits of the larger surface area and the unrestricted ion diffusion, this 3-D INPOS architecture is highly promising to serve as a scaffold in the fabrication of high-performance energy storage devices. Moreover, the facile fabrication of this highly porous 3-D INPOS architecture together with the tunable structural parameters certainly opens up new applications for the 3-D INPOS architecture such as in gas sensors and air filters.

Experimental

Preparation of 3-D INPOS and 3-D nanopore architectures

Herein, 1060 series Al alloy (99.6% purity) with a thickness of 0.3 mm was cut into several pieces with the same area of 3 cm × 2 cm, followed by electrochemically polishing under a 15 V constant voltage for 2 min. After this, they were anodized

under 200 V and at 10 °C to achieve the 3-D INPOS with a pitch and a thickness of 500 nm and 40 μm, respectively. Then, the samples were immersed in mercuric chloride ($HgCl_2$) to remove the residual Al to achieve the free-standing 3-D INPOS architectures, followed by the ion milling process to remove the barrier layer to obtain the through-pore 3-D INPOS architectures. Finally, these 3-D INPOS underwent a one-step wet etching process at 53 °C to enlarge their pore sizes to ~400 nm. To achieve the 3-D nanopores with the same structural parameters such as pitch, thickness, and pore size, a high purity Al foil (99.999%) was anodized and chemically etched under the same conditions. The anodization solution contained DI water, ethylene glycol (EG), and 85 wt% phosphoric acid (H_3PO_4) in a volume ratio of 200 : 100 : 1. The wet etching solution contained 85 wt% H_3PO_4 and DI water in a volume ratio of 1 : 19.

Fabrication of 3-D INPOS and 3-D nanopore current collectors

The 3-D INPOS and 3-D nanopore current collectors have been achieved after uniform and conform deposition of a layer of FTO *via* the cost-effective USP method, and this method has been reported in our previous report.[7] Typically, a homemade two-terminal USP equipment was used for the FTO deposition, as shown in Fig. 1b. First, the 3-D INPOS and 3-D nanopore architectures were fixed on the hot plate, and a Buchner funnel, covering these architectures, was connected to the output terminal of the USP setup. The nebulizer was used to vaporize the FTO precursor, and the compressed air was injected into the input terminal of the USP setup, carrying the vaporized FTO precursor for FTO deposition. The deposition process was conducted at 350 °C and lasted for 30 min. The FTO precursor solution was first prepared by dissolving 21 g tin(IV) chloride pentahydrate ($SnCl_4$·$5H_2O$) in 300 ml absolute ethanol. Later, 900 mg ammonium fluoride (NH_4F) was added to 10 ml DI water to form a clear and homogeneous solution. Finally, the FTO precursor was achieved after mixing these two solutions.

Fabrication of 3-D INPOS and 3-D nanopore pseudocapacitor electrodes

MnO_2, serving as the pseudocapacitive material, was deposited *via* the square wave galvanostatic electrochemical deposition at room temperature. The duty cycle of this deposition waveform was 2%, and the deposition current density was 10.3 mA cm^{-2}, normalized to the projected area. MnO_2 nanowires at different amounts ranging from 0.697 mg cm^{-2} to 2.441 mg cm^{-2} were uniformly deposited onto the 3-D INPOS and 3-D nanopore current collectors to finalize the fabrication of the pseudocapacitor electrodes. The deposition solution contained 0.01 M manganese acetate ($MnAc_2$) (98% purity) and 0.02 M ammonium acetate (NH_4Ac) (99% purity) dissolved into 90% DI water and 10% ethanol.

Assembling of the self-membrane pseudocapacitor device

Herein, two pieces of the coin cell type (CR2032) 3-D INPOS electrodes were first immersed in the 1 M Na_2SO_4 electrolyte. Afterwards, they were stacked together without further

addition of a separator. The copper wires were electrically connected to the pseudocapacitor electrode through a silver paste, and they were used as cables for electrochemical measurements. The thickness of each pseudocapacitor electrode was 20 μm (mass loading: ~1.22 mg cm^{-2}), and the entire device volume was ~1.26×10^{-2} cm^3.

Conflicts of interest

There are no conflicts to declare.

Acknowledgements

Notes and references

1   S. Chu, Y. Cui and N. Liu, *Nat. Mater.*, 2017, **16**(1), 16–22.
2   Y. Lei, *Adv. Energy Mater.*, 2016, **6**(23), 1600461.
3   N. A. Kyeremateng, T. Brousse and D. Pech, *Nat. Nanotechnol.*, 2017, **12**(1), 7–15.
4   Z. Yu, L. Tetard, L. Zhai and J. Thomas, *Energy Environ. Sci.*, 2015, **8**, 702–730.
5   P. Simon and Y. Gogotsi, *Nat. Mater.*, 2008, **7**(11), 845–854.
6   P. Simon, Y. Gogotsi and B. Dunn, *Sci. Mag.*, 2014, **343**, 1210–1211.
7   Y. Gao, Y. Lin, J. Chen, Q. Lin, Y. Wu, W. Su, W. Wang and Z. Fan, *Nanoscale*, 2016, **8**(27), 13280–13287.
8   Q. Li, Z. Wang, G. Li, R. Guo, L. Ding and Y. Tong, *Nano Lett.*, 2012, **12**(7), 3803–3807.
9   Y. He, G. Li, Z. Wang, C. Su and Y. Tong, *Energy Environ. Sci.*, 2011, **4**, 1288–1292.
10 B. Liu, B. Liu, X. Wang, X. Wu, W. Zhao, Z. Xu, D. Chen and G. Shen, *Adv. Mater.*, 2014, **26**(29), 4999–5004.
11 M. R. Lukatskaya, B. Dunn and Y. Gogotsi, *Nat. Commun.*, 2016, **7**, 12647.
12 G. Nyström, A. Marais, E. Karabulut, L. Wågberg, Y. Cui and M. M. Hamedi, *Nat. Commun.*, 2015, **6**, 7259.
13 Z. Su, C. Yang, B. Xie, Z. Lin, Z. Zhang, J. Liu, B. Li, F. Kang and C. Wong, *Energy Environ. Sci.*, 2014, **7**, 2652–2659.
14 Q. Wei, F. Xiong, S. Tan, L. Huang, E. H. Lan, B. Dunn and L. Mai, *Adv. Mater.*, 2017, 1602300.
15 F. Grote, R. Kühnel, A. Balducci and Y. Lei, *Appl. Phys. Lett.*, 2014, **104**(5), 053904.
16 Y. Gao, H. Jin, Q. Lin, X. Li, M. M. Tavakoli, S. Leung, W. M. Tang, L. Zhou, H. L. W. Chan and Z. Fan, *J. Mater. Chem. A*, 2015, **3**(19), 10199–10204.
17 F. Grote and Y. Lei, *Nano Energy*, 2014, **10**, 63–70.
18 X. Xiao, T. Ding, L. Yuan, Y. Shen, Q. Zhong, X. Zhang, Y. Cao, B. Hu, T. Zhai and L. Gong, *Adv. Energy Mater.*, 2012, **2**(11), 1328–1332.
19 C. Xu, Z. Li, C. Yang, P. Zou, B. Xie, Z. Lin, Z. Zhang, B. Li, F. Kang and C. Wong, *Adv. Mater.*, 2016, **28**(21), 4105–4110.
20 Z. Yu, B. Duong, D. Abbitt and J. Thomas, *Adv. Mater.*, 2013, **25**(24), 3302–3306.
21 Z. Zhang, L. Wang, Y. Li, Y. Wang, J. Zhang, G. Guan, Z. Pan, G. Zheng and H. Peng, *Adv. Energy Mater.*, 2016, **7**(5), 1601814.
22 C. Zhu, L. Yang, J. K. Seo, X. Zhang, S. Wang, J. Shin, D. Chao, H. Zhang, Y. S. Meng and H. J. Fan, *Mater. Horiz.*, 2017, **4**, 415–422.
23 H. Zhao, C. Wang, R. Vellacheri, M. Zhou, Y. Xu, Q. Fu, M. Wu, F. Grote and Y. Lei, *Adv. Mater.*, 2014, **26**(45), 7654–7659.
24 C. Liu, E. I. Gillette, X. Chen, A. J. Pearse, A. C. Kozen, M. A. Schroeder, K. E. Gregorczyk, S. B. Lee and G. W. Rubloff, *Nat. Nanotechnol.*, 2014, **9**(12), 1031–1039.
25 Y. Lin, Q. Lin, X. Liu, Y. Gao, J. He, W. Wang and Z. Fan, *Nanoscale Res. Lett.*, 2015, **10**(1), 495.
26 X. Chen, E. Pomerantseva, P. Banerjee, K. Gregorczyk, R. Ghodssi and G. Rubloff, *Chem. Mater.*, 2012, **24**(7), 1255–1261.
27 L. Gu, M. M. Tavakoli, D. Zhang, Q. Zhang, A. Waleed, Y. Xiao, K. Tsui, Y. Lin, L. Liao and J. Wang, *Adv. Mater.*, 2016, **28**(44), 9713–9721.
28 I. S. Molchan, T. V. Molchan, N. V. Gaponenko, P. Skeldon and G. E. Thompson, *Electrochem. Commun.*, 2010, **12**(5), 693–696.
29 X. Sun, Q. Li, Y. Lü and Y. Mao, *Chem. Commun.*, 2013, **49**(40), 4456–4458.
30 J. Maeng, Y. Kim, C. Meng and P. P. Irazoqui, *ACS Appl. Mater. Interfaces*, 2016, **8**(21), 13458–13465.
31 L. Wen, Y. Mi, C. Wang, Y. Fang, F. Grote, H. Zhao, M. Zhou and Y. Lei, *Small*, 2014, **10**(15), 3162–3168.
32 K. Qin, E. Liu, J. Li, J. Kang, C. Shi, C. He, F. He and N. Zhao, *Adv. Energy Mater.*, 2016, **6**(18), 1600755.
33 X. Xiao, X. Peng, H. Jin, T. Li, C. Zhang, B. Gao, B. Hu, K. Fu and J. Zhou, *Adv. Mater.*, 2013, **25**(36), 5091–5097.
34 Z. Yu and J. Thomas, *Adv. Mater.*, 2014, **26**(25), 4279–4285.
35 X. Lu, M. Yu, G. Wang, T. Zhai, S. Xie, Y. Ling, Y. Tong and Y. Li, *Adv. Mater.*, 2013, **25**(2), 267–272.
36 Y. Ahn, J. Park, D. Shin, S. Cho, S. Park, H. Kim, Y. Piao, J. Yoo and Y. Kim, *J. Mater. Chem. A*, 2015, **3**(20), 10715–10719.